

MORPHOLOGY OF THE GALAXY DISTRIBUTION FROM WAVELET DENOISING

VICENT J. MARTÍNEZ

Observatori Astronòmic, Universitat de València, Apartat de Correus 22085, E-46071 València, Spain

JEAN-LUC STARCK

CEA-Saclay, DAPNIA/SEDI-SAP, Service d'Astrophysique, F-91191 Gif sur Yvette, France

ENN SAAR

Tartu Observatoorium, Tõravere, 61602, Estonia

DAVID L. DONOHO

Department of Statistics, Stanford University, Sequoia Hall, Stanford, CA 94305, USA

SIMON REYNOLDS

Blackett Laboratory, Imperial College London, SW7 2AZ, UK

PABLO DE LA CRUZ

Observatorio Astronómico, Universidad de Valencia, Apartado de Correos 22085, E-46071 Valencia, Spain

AND

SILVESTRE PAREDES

Departamento de Matemática Aplicada y Estadística, Universidad Politécnica de Cartagena, 30203 Cartagena, Spain

Submitted for publication to ApJ

ABSTRACT

We have developed a method based on wavelets to obtain the true underlying smooth density from a point distribution. The goal has been to reconstruct the density field in an optimal way ensuring that the morphology of the reconstructed field reflects the true underlying morphology of the point field which, as the galaxy distribution, has a genuinely multiscale structure, with near-singular behavior on sheets, filaments and hotspots. If the discrete distributions are smoothed using Gaussian filters, the morphological properties tend to be closer to those expected for a Gaussian field. The use of wavelet denoising provide us with a unique and more accurate morphological description.

Subject headings: methods: statistical; galaxies: clustering; large-scale structure of Universe

1. INTRODUCTION

The large-scale structure of the universe shows intricate patterns with filaments, clusters, and sheet-like arrangements of galaxies encompassing large nearly empty regions, the so-called voids. This complex structure shows clearly non-Gaussian features. However, it is likely that the observed structure developed from tiny fluctuations of an initial Gaussian random field by the action of gravity. This is the scenario suggested by the analysis of the maps of the microwave background radiation. Thus, it is important to check if the present large-scale structure is compatible with the Gaussianity of the initial fluctuations.

Different statistical measures have been used in the cosmological literature to quantitatively describe the cosmic texture (Martínez & Saar 2002). To complement the

information provided by the second-order descriptors – the correlation function and the power spectrum – different alternatives have been proposed. Some of these statistics are focused in quantifying geometrical and morphological aspects of the distribution. In this context, the *genus*, introduced to measure deviations from Gaussianity (Gott et al. 1986), is one of the most widely used techniques. The genus and its generalization, the Minkowski functionals, allow us to quantify the morphology of the isodensity surfaces of the matter distribution.

The Minkowski functionals describe the morphology of hypersurfaces, with dimensionality one less than that of the encompassing space. In the analysis of the three-dimensional matter distribution, the functionals are applied to isodensity surfaces separating regions with density above and below a given threshold. This implies that the first step is to obtain a smooth density field from the discrete distribution of matter. The morphological descriptors can be applied both to the observed galaxy distribution and to the dark-matter based N -body simulations of the large-scale structure. In all cases, we have to smooth the data to construct a real density field. This smoothing has to be more severe, when we want to mea-

Electronic address: martinez@uv.es
Electronic address: jstarck@cea.fr
Electronic address: saar@aai.ee
Electronic address: donoho@stat.stanford.edu
Electronic address: simon.reynolds@imperial.ac.uk
Electronic address: pablo.cruz@uv.es
Electronic address: silvestre.paredes@upct.es

sure the morphology of a discrete point distribution as a redshift catalog, than when we measure the morphology of the dark matter distribution in cosmological simulations.

The first assumption we have to make is that the galaxy distribution is a sample from a Cox process (see, e.g., Martínez & Saar (2002)); the galaxy positions $(x_i, y_i, z_i), i = 1, \dots, n$ represent a point process which samples the continuous field. Smoothing has to reconstruct the underlying $f(x, y, z)$, and if the smoothing is done either well or poorly, then the estimated field \hat{f} will be either good or bad at representing the true underlying field f .

It is well known that when we are estimating a density field f , there is a critical smoothing level at which it begins to be true that the estimated field resembles the true field. For example, with a C^2 density in dimension 1, we need to smooth with the bandwidth

$$h_n \sim an^{-1/5}, \quad (1)$$

where a depends on the underlying density field f (Donoho 1988). If we smooth less than this, $h < h_n$, then the number of modes of the estimate \hat{f} will tend to infinity, while if we smooth more than this, the estimate will have fewer modes than the true density (Silverman 1981).

Cosmological density fields, instead of being a generic C^2 field, are more complex in nature. They have a genuinely multiscale structure, with near-singular behavior in sheets, filaments and clusters. The smoothing procedures that are proper for such objects are presumably entirely different than the smoothing that is good for C^2 objects, and so we do not expect that Eq. 1 can be applied in this setting.

Correct smoothing should also be spatially adaptive, so that locally it is using a scale based on the degree of smoothness of the object, or the scale should be smaller than the statistically significant structures. The method advocated in this paper, based on wavelet thresholding, does this automatically and provides a smoothing recipe that is unique for a given realization of a point process and does not depend on an a priori chosen bandwidth.

Having obtained a consistent estimate of the density field, we can be certain that the morphology of the reconstructed field reflects the true underlying morphology of the point field. The goal of the present paper is finding and analyzing such morphological descriptors.

2. SMOOTHING SCHEMES

In this section we will introduce two different smoothing techniques that can be applied to obtain a continuous density field from a discrete point distribution. Our goal is to analyze how these schemes affect the correct determination of the Minkowski functionals, and which is the best to study the morphology of the matter distribution.

2.1. Gaussian smoothing

For morphological studies, smoothing is typically done by using a Gaussian kernel

$$W(\mathbf{x}) = \frac{1}{(2\pi)^{3/2}\sigma^3} \exp\left(-\frac{\mathbf{x}^2}{2\sigma^2}\right). \quad (2)$$

The window width σ is the parameter that governs the level of smoothing of the discrete data to obtain the

kernel density estimate. Hamilton et al. (1986) recommend that the smoothing length has to be chosen larger than the correlation length, r_0 , the distance at which the two-point correlation function $\xi(r_0) = 1$. This is the recipe that is usually used for the morphological analysis of the observed galaxy distribution, together with a requirement that the smoothing length should also be larger than the typical size of the volume-per-galaxy¹ $d = (V/n)^{1/3}$, where V is the total volume of the sample and n the number of points (galaxies) (see, e.g., Hoyle et al. (2002)).

A lot of work has been done by the statistical community on the optimal smoothing length that would give the best density estimate. However, as Silverman (1981) has pointed out: “Most methods seem to depend on some arbitrary choice of the scale of the effects being studied”. Certainly to choose the appropriate value of σ is an art, but in any case we must avoid two kinds of artifacts: undersmoothing, which causes huge numbers of spurious oscillations and oversmoothing, which removes real features of structure. This last aspect is crucial when measuring the morphology of the large scale structure because, since smoothing has to be large enough to describe morphology reliably, it will inevitably erase small-scale non-Gaussian features. Coles & Lucchin (1995) note that “smoothing on scales much larger than the scale at which correlations are significant will tend to produce a Gaussian distribution by virtue of the central limit theorem” (Martínez et al. 1993). A conservative approach is based on searching for efficient and consistent estimates of the bandwidth that are typically upper bounds. These scales would reveal as much detail as the optimal bandwidth, if it exists (Donoho 1988).

2.2. Wavelet denoising

The Undecimated Isotropic Wavelet Transform (UIWT), also named *à trous algorithm*, decomposes an $n \times n \times n$ data set D as a superposition of the form

$$D = c_J + \sum_{j=1}^J w_j,$$

where c_J is a coarse or smooth version of the original data D and w_j represents the details of D at scale 2^{-j} (see Starck et al. (1998); Starck & Murtagh (2002) for details). Thus, the algorithm outputs $J + 1$ sub-band arrays of size $n \times n \times n$. We will use an indexing convention such that $j = 1$ corresponds to the finest scale (high frequencies). Wavelets have been used successfully for denoising via non-linear filtering or thresholding methods (Starck & Murtagh 2002). Hard thresholding, for instance, consists of setting all insignificant coefficients (*i.e.* coefficients with an absolute value below a given threshold) to zero.

For the noise model, given that this relates to point pattern clustering, we have to consider the Poisson noise case. The autoconvolution histogram method (Slezak et al. 1993) used for X-ray image (Starck & Pierre 1998; Pierre et al. 2004; Valtchanov et al. 2004) can also be used here. It consists of calculating numerically the probability distribution function (pdf) of a wavelet $w_{j,x,y,z}$ coefficient with the

¹ d is typically referred to as the mean interparticle separation.

hypothesis that the galaxies used for obtaining $w_{j,x,y,z}$ are randomly distributed. The pdf is obtained by autoconvolving n times the histogram of the wavelet function, n being the number of galaxies which have been used for obtaining $w_{j,x,y,z}$, i.e. the number of galaxies in a box around (x, y, x) , the size of the box depending on the scale j . More details can be found in Starck & Pierre (1998); Starck & Murtagh (2002).

Once the pdf relative to the coefficient $w_{j,x,y,z}$ is known, we can detect the significant wavelet coefficients easily. We derive two threshold values $T_{j,x,y,z}^{min}$ and $T_{j,x,y,z}^{max}$ such that

$$\begin{aligned} \text{Prob}(W < T_{j,x,y,z}^{min}) &= \epsilon \\ \text{Prob}(W > T_{j,x,y,z}^{max}) &= \epsilon \end{aligned} \quad (3)$$

ϵ corresponding to the confidence level, and the positive (respective negative) wavelet coefficient is significant if it is larger than $T_{j,x,y,z}^{max}$ (resp. lower than $T_{j,x,y,z}^{min}$). Denoting D the noisy data and δ the thresholding operator, the filtered data \tilde{D} are obtained by :

$$\tilde{D} = \mathcal{R}\delta(\mathcal{T}D) \quad (4)$$

where \mathcal{T} is the wavelet transform operator and \mathcal{R} is the wavelet reconstruction operator. In practice, we get better results using the iterative reconstruction described in Starck & Murtagh (2002) which minimizes the l_1 norm of the wavelet coefficients. It is this iterative technique that we have used for our experiments.

Poisson noise denoising has been addressed in a series of recent papers (Fryźlewicz & Nason 2004; Kolaczyk 2000, 1999; Nowak & Baraniuk 1999; Antoniadis & Sapatinas 2001; Timmermann & Nowak 1999; Jammal & Bijaoui 2004). All of them uses the Haar wavelet transform because it presents the interesting property that a Haar wavelet coefficient is the difference between two variables which follow a Poisson distribution. This property allows us to derive an analytical form of the pdf of the wavelet coefficients. The Haar transform has however several drawbacks such block artifact creation or a tendency to create square structures. For XMM, it was also shown than the isotropic wavelet transform was much more powerful for detecting clusters of galaxies (Valtchanov et al. 2001).

3. MORPHOLOGICAL DESCRIPTORS

3.1. The genus curve

Historically, the first morphological descriptor used was the genus (Gott et al. 1986). The genus $G(S)$ measures the connectivity of a surface, S , with holes and disconnected pieces, by the difference of the number of holes and the number of isolated regions:

$$G(S) = \text{number of holes} - \text{number of isolated regions} + 1.$$

The genus of a sphere is $G = 0$, a torus or a sphere with a handle have the genus $G = +1$, a sphere with N handles has the genus $G = +N$, while the collection of N disjoint spheres has the genus $G = -(N - 1)$. The genus describes the topology of the isodensity surfaces, thus its study is in the cosmological literature frequently called “topological analysis”.

The genus curve is usually parameterized by two related quantities, the filling factor, f , which is the fraction of the survey volume above the density threshold or,

alternatively, by the quantity ν defined by

$$f = \frac{1}{\sqrt{2\pi}} \int_{\nu}^{\infty} e^{-t^2/2} dt. \quad (5)$$

In the case of a Gaussian random field, ν is also the number of standard deviations by which the threshold density departs from the mean density, and with this parametrization, the genus per unit volume of a surface, S , corresponding to a given density threshold, $g \equiv (G(S) - 1)/V$, follows the analytical expression

$$g(\nu) = N(1 - \nu^2) \exp\left(-\frac{\nu^2}{2}\right), \quad (6)$$

where the amplitude N depends on the power spectrum of the random field (Hamilton et al. 1986). If the density distribution is not Gaussian, the parameterization (5) eliminates the (trivial) non-Gaussianity caused by the one-point density distribution. Opinions differ about which argument is better; we shall use ν in this paper.

This curve, symmetric about 0 in ν , is typical of the random-phase morphology. We have simulated a Gaussian random field with a power-law spectrum $P(k) \sim k^{-1}$ and this field has been smoothed with a Gaussian kernel with $\sigma = 3$ (the cube size is 128). As we see in Fig. 1 (left panels), the regions with density above or below the mean value are statistically indistinguishable. In the right column of this figure we show the isodensity surfaces for our realization, which encompass the denser regions of the simulated box. The three panels, from top to bottom, correspond respectively to 7%, 50%, and 93% of the volume encompassing regions with higher density. Likewise, the left column shows the low-density regions corresponding to the same percentage of the volume. The symmetry between the high-density and the low-density regions is clearly seen. The right panels of Fig. 1 depict the same realization, but more heavily smoothed, with the smoothing length $\sigma = 8$. These are the standard distributions, which are typically compared with observational data. Such a morphology is usually called “the sponge morphology”. The sponginess of the isodensity surfaces is clearly seen, particularly at the central pair of panels, in both figures, corresponding to the 50% low and high densities: the surface separating both regions has many holes, is multiply connected, and has negative curvature.

Other types of genus curves can be found in the cosmological literature. When rich clusters dominate the distribution, the genus curves are shifted to the left, and the morphology is referred to as “meat-ball”, while the expression “Swiss-cheese” is used for right-shifted genus curves corresponding to distributions with empty bubbles surrounded by a single high density region.

3.2. Minkowski functionals

An elegant generalization of the genus statistic is to consider this measure as one of the four Minkowski functionals which describe different morphological aspects of the galaxy distribution (Mecke et al. 1994). These functionals provide a complete family of morphological measures – all additive, motion invariant and conditionally continuous functionals defined for any hypersurface are linear combinations of its Minkowski functionals.

The Minkowski functionals (MF for short) describe the morphology of isodensity surfaces (Minkowski 1903;

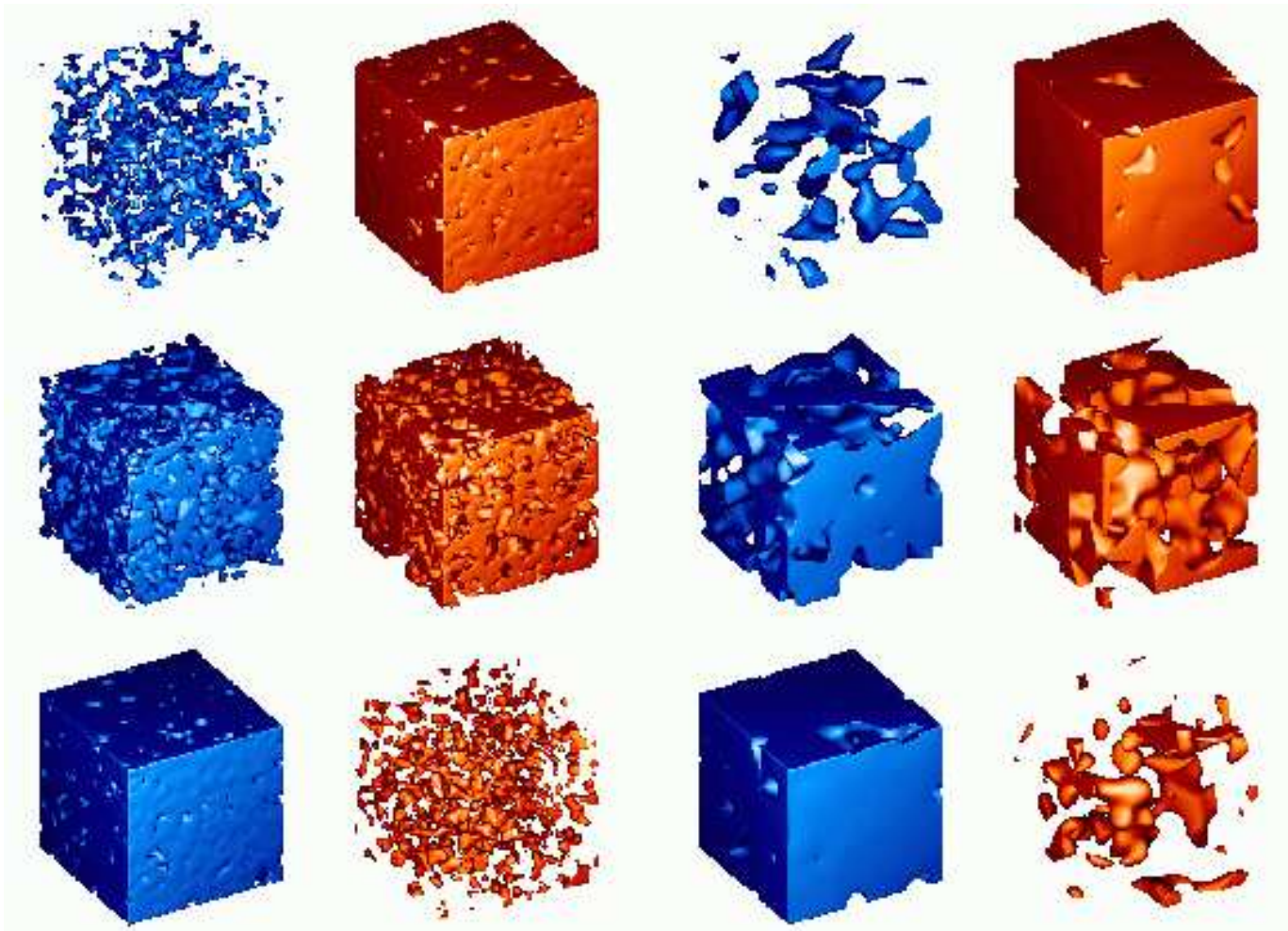


FIG. 1.— The two columns on the left show the spatial distribution of the low- (first column) and high density (second column) regions for a realization of a Gaussian random field, with comparatively little smoothing ($\sigma = 3$). The upper pair shows the 7% (volume fraction) low, 93% high density regions, the middle pair stands for 50%-50%, and the lower pair shows the 93% low-density, 7% high-density case. The two columns on the right are the same, but for heavy smoothing ($\sigma = 8$).

Tomita 1990), and depend thus on two factors – the smoothing procedure and the specific density level, (see Sheth & Sahni (2005) for a recent review). An alternative approach starts from the point field, decorating the points with spheres of the same radius, and studying the morphology of the resulting surface (Schmalzing et al. 1996; Kerscher et al. 1997). These functionals depend only on one parameter (the radius of the spheres), but this approach does not refer to a density; we shall not use that for the present study.

The Minkowski functionals are defined as follows. Consider an excursion set F_ϕ of a field $\phi(\mathbf{x})$ in 3-D (the set of all points where $\phi(\mathbf{x}) \geq \phi$). Then, the first Minkowski functional (the volume functional) is the volume of the excursion set:

$$V_0(\phi) = \int_{F_\phi} d^3x.$$

The second MF is proportional to the surface area of the boundary δF_ϕ of the excursion set:

$$V_1(\phi) = \frac{1}{6} \int_{\delta F_\phi} dS(\mathbf{x}).$$

The third MF is proportional to the integrated mean

curvature of the boundary:

$$V_2(\phi) = \frac{1}{6\pi} \int_{\delta F_\phi} \left(\frac{1}{R_1(\mathbf{x})} + \frac{1}{R_2(\mathbf{x})} \right) dS(\mathbf{x}),$$

where R_1 and R_2 are the principal curvatures of the boundary. The fourth Minkowski functional is proportional to the integrated Gaussian curvature (the Euler characteristic) of the boundary:

$$V_3(\phi) = \frac{1}{4\pi} \int_{\delta F_\phi} \frac{1}{R_1(\mathbf{x})R_2(\mathbf{x})} dS(\mathbf{x}).$$

The last MF is simply related to the morphological genus g introduced in the previous subsection by

$$V_3 = \chi = \frac{1}{2}(1 - G)$$

(χ is the usual notation for the Euler characteristic). The functional V_3 is a bit more comfortable to use – it is additive, while G is not, and it gives just twice the number of isolated balls (or holes). Although the genus continues to be widely used, in several recent papers many authors have chosen to present the Minkowski functional V_3 ; we

shall follow this recent and logical trend. Instead of the functionals, their spatial densities V_i are frequently used:

$$v_i(f) = V_i(f)/V, \quad i = 0, \dots, 3,$$

where V is the total sample volume.

All the Minkowski functionals have analytic expressions for isodensity slices of realizations of Gaussian random fields. For three-dimensional space they are:

$$\begin{aligned} v_0 &= \frac{1}{2} - \frac{1}{2} \Phi\left(\frac{\nu}{\sqrt{2}}\right), \\ v_1 &= \frac{2}{3} \frac{\lambda}{\sqrt{2\pi}} \exp\left(-\frac{\nu}{2}\right), \\ v_2 &= \frac{2}{3} \frac{\lambda^2}{\sqrt{2\pi}} \nu \exp\left(-\frac{\nu}{2}\right), \\ v_3 &= \frac{\lambda^3}{\sqrt{2\pi}} (\nu^2 - 1) \exp\left(-\frac{\nu}{2}\right), \end{aligned}$$

where $\Phi(\cdot)$ is the Gaussian error integral, and λ is determined by the correlation function $\xi(r)$ of the field as:

$$\lambda^2 = \frac{1}{2\pi} \frac{\xi''(0)}{\xi(0)}.$$

3.3. Numerical algorithms

Several algorithms are used to calculate the Minkowski functionals for a given density field and a given density threshold. We can either try to follow exactly the geometry of the isodensity surface, e.g., using triangulation (Sheth et al. 2003), or to approximate the excursion set on a simple cubic lattice. The algorithm that was proposed first by Gott et al. (1986), uses a decomposition of the field into filled and empty cells, and another popular algorithm (Coles et al. 1996) uses a grid-valued density distribution. The lattice-based algorithms are simpler and faster, but not as accurate as the triangulation codes. The main difference is in the edge effects – while surface triangulation algorithms do not suffer from these, edge effects may be rather serious for the lattice algorithms.

We use a simple grid-based algorithm, based on integral geometry (the Crofton's intersection formula, see Schmalzing & Buchert (1997)). We find the density thresholds for given filling fractions by sorting the grid densities, first. Vertices with higher densities than the threshold form the excursion set. This set is characterized by its basic sets of different dimensions – points (vertices), edges formed by two neighboring points, squares (faces) formed by four edges, and cubes formed by six faces. The algorithm counts the numbers of all basic sets, and finds the values of the Minkowski functionals as

$$\begin{aligned} V_0(f) &= a^3 N_3, \\ V_1(f) &= a^2 \left(\frac{2}{9} N_2(f) - \frac{2}{3} N_3(f) \right), \\ V_2(f) &= a \left(\frac{2}{9} N_1(f) - \frac{4}{9} N_2(f) + \frac{2}{3} N_3(f) \right), \\ V_3(f) &= N_0(f) - N_1(f) + N_2(f) - N_3(f), \end{aligned}$$

where a is the grid step, f is the filling factor, N_0 is the number of vertices, N_1 is the number of edges, N_2 is the number of squares (faces), and N_3 is the number of basic

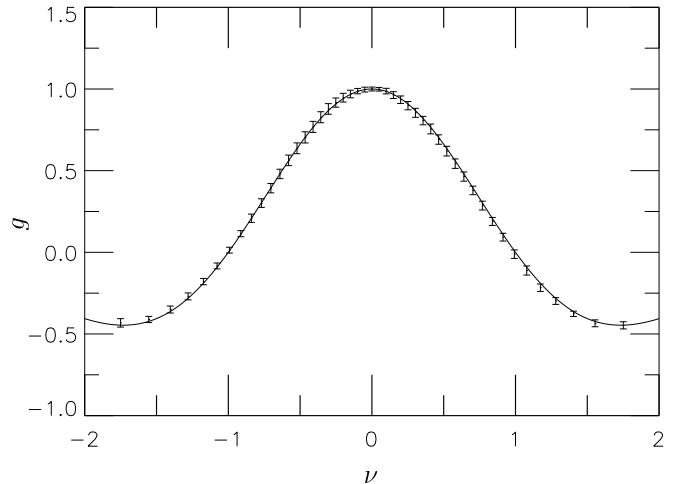


FIG. 2.— The average genus curve for 50 realizations of a Gaussian random field with $P(k) \sim k^{-1}$ together with the expected analytical result (solid line). The error bars show 1σ deviations.

cubes in the excursion set for a given filling factor (density threshold). This formula was proven by Adler (1981) and was first used in cosmological studies by Coles et al. (1996); we refer to that paper for a thorough discussion of the method and of necessary boundary corrections.

This algorithm is simple to program, and it gives excellent results, provided the grid step is substantially smaller than the characteristic lengths of the isosurfaces (the smoothing length). This is needed to be able to accurately follow the geometry of the surface. It is also very fast, allowing the use of Monte-Carlo simulations for error estimation.

In order to test the algorithm and our program, we calculated the genus curve for 50 realizations of a Gaussian random field with a power-law power spectrum $P(k) \sim k^{-1}$ in a 128^3 box. The realizations were smoothed with a Gaussian kernel of $\sigma = 3$. The results are shown in Fig. 2. Our results are very close to the theoretical expectations, and the errors are similar to those reported recently by Sheth et al. (2003), who used a very precise algorithm based on triangulated surfaces (SURFGEN).

4. MINKOWSKI FUNCTIONALS OF SIMULATED POINT DISTRIBUTIONS

In this section, we apply Gaussian smoothing and wavelet denoising procedures to three different point sets. For the Gaussian kernel, we choose different values of the bandwidth σ . The fourth Minkowski functional (the Euler-Poincaré characteristic V_3) is then calculated for the smoothed density fields. We will see how the Gaussian smoothing tends to bring the V_3 -curve closer to the expected one for a Gaussian random field, independently of the characteristics of the initial field. It demonstrates that the morphological characteristics, obtained by Gaussian smoothing, may carry more information about the filter itself than about the point process. We have chosen different point processes with genuinely non-Gaussian features, and with different topologies.

4.1. Description of the samples

The first data set used in this analysis has been generated by A. Klypin from an N -body simulation, and has

TABLE 1
SIMULATED POINT DISTRIBUTIONS.

	N	L	r_0	d	r'_0	d'	$\langle \text{nnd}' \rangle$
nbody	14616	60	4.0	2.45	8.5	5.2	4.5
filaments	14718	100	10.0	4.1	12.8	5.2	2.6
cheese	14718	128	27.8	5.2	27.8	5.2	1.1

Note: The first three lengths (L , r_0 and d) are in units of h^{-1} Mpc, the last three lengths (r'_0 , d' and $\langle \text{nnd}' \rangle$), in grid units.

been used in wavelet applications before (see, e.g. Starck & Murtagh 2002, p. 221). This simulation is described by Klypin & Holtzman (1997). It contains 14616 galaxies within a cube of size of $60h^{-1}$ Mpc. All the three samples have similar number of data points, and we calculate the Minkowski functionals for all three samples, using a 128^3 mesh. The correlation length r_0 and the size of the volume per particle d for this sample, both in physical and grid units, are given in Table 1. We also give the mean nearest-neighbor distance for the sample ($\langle \text{nnd}' \rangle$). If a sample is not too heavily clustered, this should be close to d .

The second point process is based on Voronoi tessellation. We generate a Voronoi tessellation similar to the observed large-scale galaxy distribution, with the mean size of cells of $40h^{-1}$ Mpc in a $100h^{-1}$ Mpc cube, and populate the edges of the cells (filaments). There are about 26 Voronoi cells; the sample contains 14718 points, all close to filaments, with a r^{-2} cross-section density profile, and a $3h^{-1}$ Mpc density scale. About 70–75% of the space is empty. Table 1 gives the characteristic lengths for this sample.

We will call the third data set the “Swiss cheese” model. In a 128^3 cube, we cut out 40 holes with radii R in $[20, 40]$, with a uniform distribution of hole volumes. About 80–83% of the sample volume is empty, the remaining volume is filled with a Poisson distribution of about 15000 points (see Table 1).

These simulated galaxy distributions are shown in Fig. 3.

4.2. Smoothing and morphology

In order to find the morphological descriptors (Minkowski functionals) for our realizations of point processes we have to smooth the data to obtain a continuous density field. The usual approach is to use Gaussian kernels for smoothing; we shall compare the results with those obtained by the wavelet-based smoothing scheme introduced in this paper. We calculated all MF-s, but as the functional V_3 shows more details than others, we show only the results for this functional here. Fig. 4 shows, in the panels of the right column, the three point patterns of Fig. 3 filtered by the 3D wavelet transform, using the algorithm described previously. The left and the middle panels of each row correspond to Gaussian smoothing with $\sigma = 1$ and $\sigma = 3$ (in grid units), respectively.

We can clearly see that when the bandwidth is too small (left panels), discreteness and noise dominate the reconstructed density fields, while using a larger value of σ tends to erase all the small scale features of the distribution. This is also shown in Fig. 5, where we can see that the morphology of the Gaussian-smoothed den-

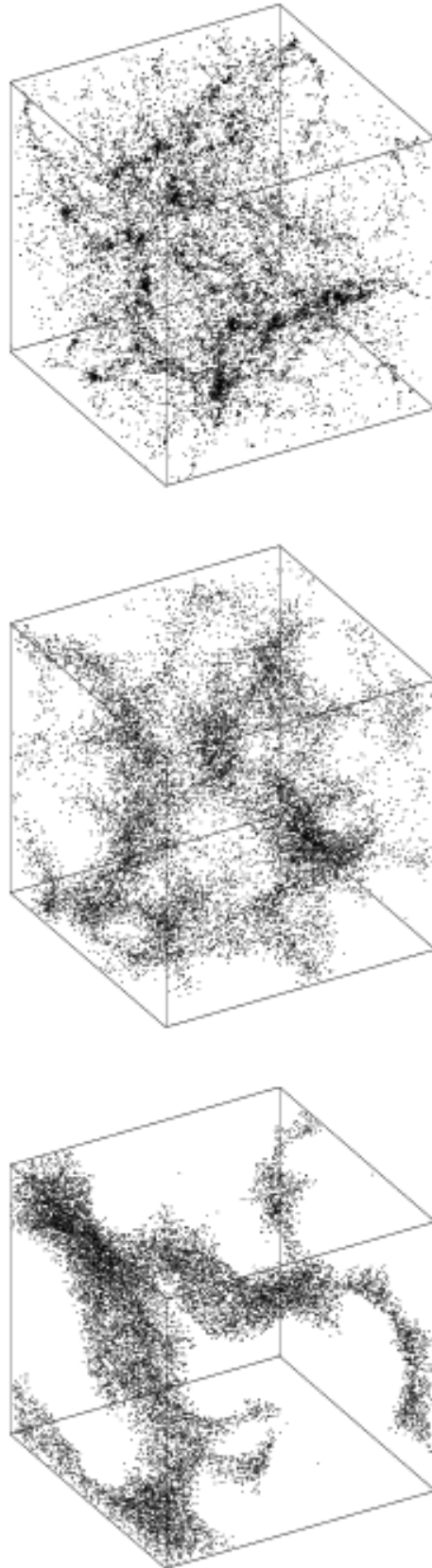


FIG. 3.— The three data sets that will serve to illustrate the different smoothing schemes and their implications when estimating the Euler characteristic. The top panel shows the N -body data, the middle panel shows the Voronoi filament model, and the bottom panel – the nearly-empty Swiss cheese model.

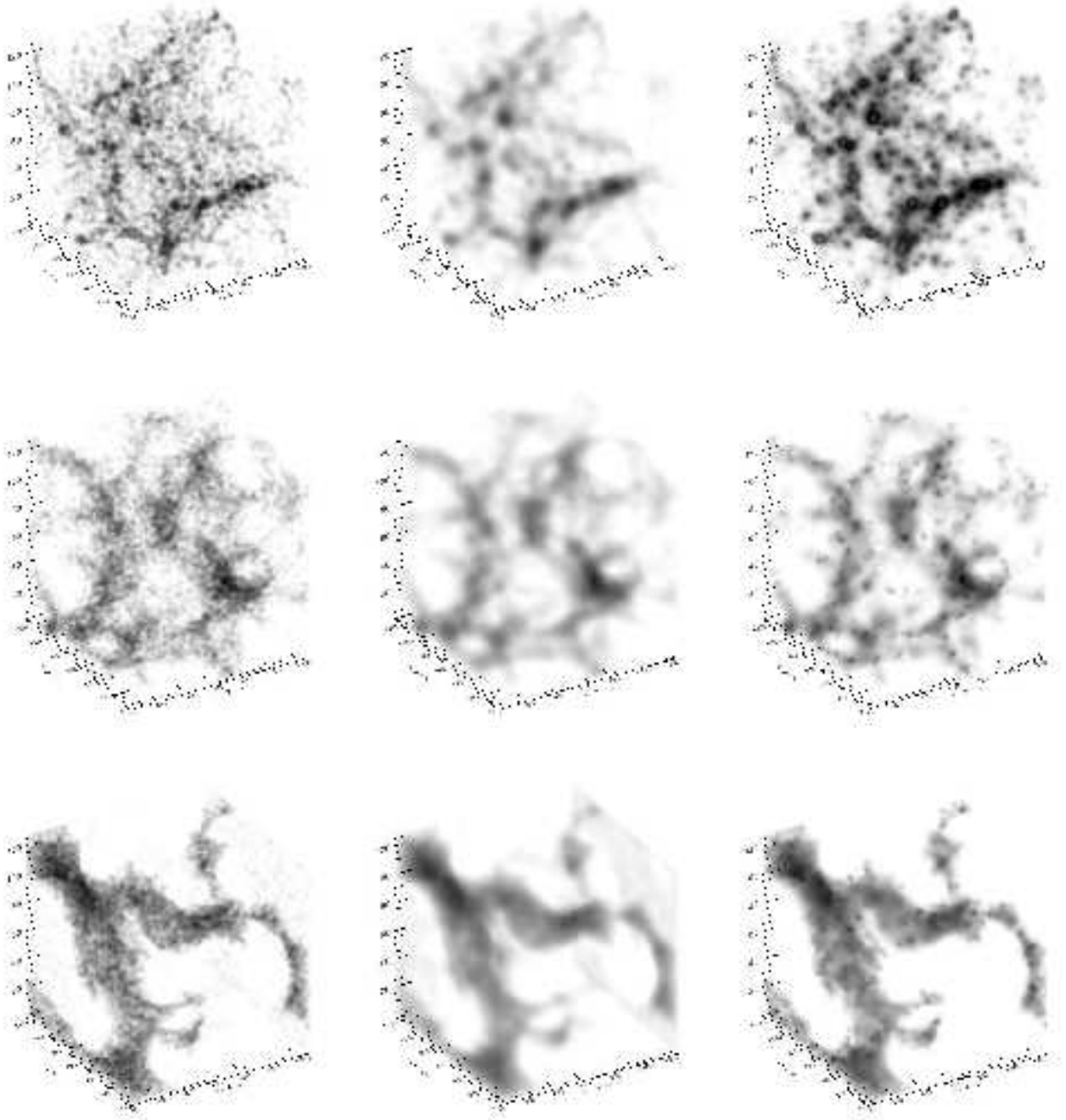


FIG. 4.— Rendering of the density fields, obtained by smoothing of the three data sets shown in Fig. 3 with a Gaussian filter with $\sigma = 1$ (first column), $\sigma = 3$ (second column) by and wavelet denoising (third column). The smoothing lengths are given in grid units.

sity field, as described by the Euler characteristic V_3 , depends strongly on the width of the Gaussian filter. This width is a free parameter and thus the Gaussian-filtered density field is not uniquely determined. Choosing the width of the filter we discard information on scales of that width and smaller. On the other hand, the wavelet transform leads to a sparse representation of the density field and allows us to detect and keep at all scales coefficients which have the greatest probability to be real. This is demonstrated by the 3D image in the right panels of Fig. 4, where we see, e.g., in the rendering of the N -body model (top-right) how large filaments, big clus-

ters and walls coexist with small scale features such as the density enhancements around groups and small clusters. The Euler characteristic of this adaptive reconstructed density field is much more informative, because it is unique, it does not depend on the particular choice of the filter radius. Because of that, wavelet morphology is clearly a more useful tool than the usual approach of Gaussian smoothing. Also, the Minkowski functionals of Gaussian-smoothed density fields mimic those of Gaussian random fields, in contrast with the wavelet-based approach. Thus, they describe more the properties of the filter, than the real morphology of the density distri-

bution.

This is seen already in the case of the N -body model (the top panel of Fig. 5), where the V_3 curve is close to Gaussian already for $\sigma = 3$ (in grid units), much smaller than r_0 , and even smaller than the mean nearest-neighbor distance.

For the clearly non-Gaussian Voronoi filament model, when we increase the value of σ , the V_3 curves also approach the typical shape for a Gaussian field (see the middle panel of Fig. 5), while the wavelet-denoised density shows the expected behavior for the Euler characteristic for this kind of spatial configuration. The three curves shown in the middle panel of Fig. 5 correspond to the iso-density contours shown in Fig. 6. While for Gaussian smoothing with $\sigma = 3$ it is still possible to see the filamentary structure in the V_3 diagram, for $\sigma = 8$ the isocountours are indistinguishable of those of a Gaussian field like the one shown in Fig. 1. It is clear that such a smoothing is excessive, and destroys the original morphology of the point sample. The V_3 curve is, in fact, close to Gaussian for $\sigma = 6$ already. Both $\sigma = 6$ and $\sigma = 8$ are smaller than the correlation length of this sample (see Table 1), and $\sigma = 6$ is close to the size of the volume-per-particle d .

The nearly-empty Swiss cheese model is even more non-Gaussian, and therefore, even for large values of σ , Gaussian smoothing does not converge to the symmetric V_3 curve. Nevertheless, the shape of the curve for the Gaussian-smoothed density depends strongly on the bandwidth, and again the curve for the wavelet-denoised density is clearly more representative of the true underlying morphology.

5. MORPHOLOGY OF THE 2DFGRS

5.1. Data

The best available redshift catalog to study morphology of the galaxy distribution at present is the 2dF Galaxy Redshift Survey (2dFGRS) (Colless et al. 2003). It fills large compact volume(s) in space and includes more than a quarter of million of galaxies. This is a flux-limited catalog and therefore the density of galaxies decreases with distance. For statistical analysis of such of surveys, a weighting scheme that compensates for the missing galaxies at large distances, has to be used. Usually, each galaxy is weighted by the inverse of the selection function (Martínez & Saar 2002). However, the resulting densities will have different resolution at different locations, and will not be suitable for morphological studies.

At the cost of discarding many surveyed galaxies, one can alternatively use volume-limited samples. In this case, the variation in density at different locations depends only on the fluctuations of the galaxy distribution itself. We have used the volume-limited samples prepared by the 2dF team for scaling studies (Croton et al. 2004a,b), and kindly sent to us by Darren Croton. As our basic sample, we chose the catalog with absolute luminosities in the range $-19 > M_{B_j} - 5 \log_{10} h > -20$ (the type dependent $k + e$ correction (Norberg et al. 2002) has been applied to the magnitudes). This sample contains galaxies with luminosity around L_* . This catalog is the largest of the 2dF volume-limited catalogs, and as Baugh et al. (2004) point out, it provides optimal balance between the surveyed volume and the number den-

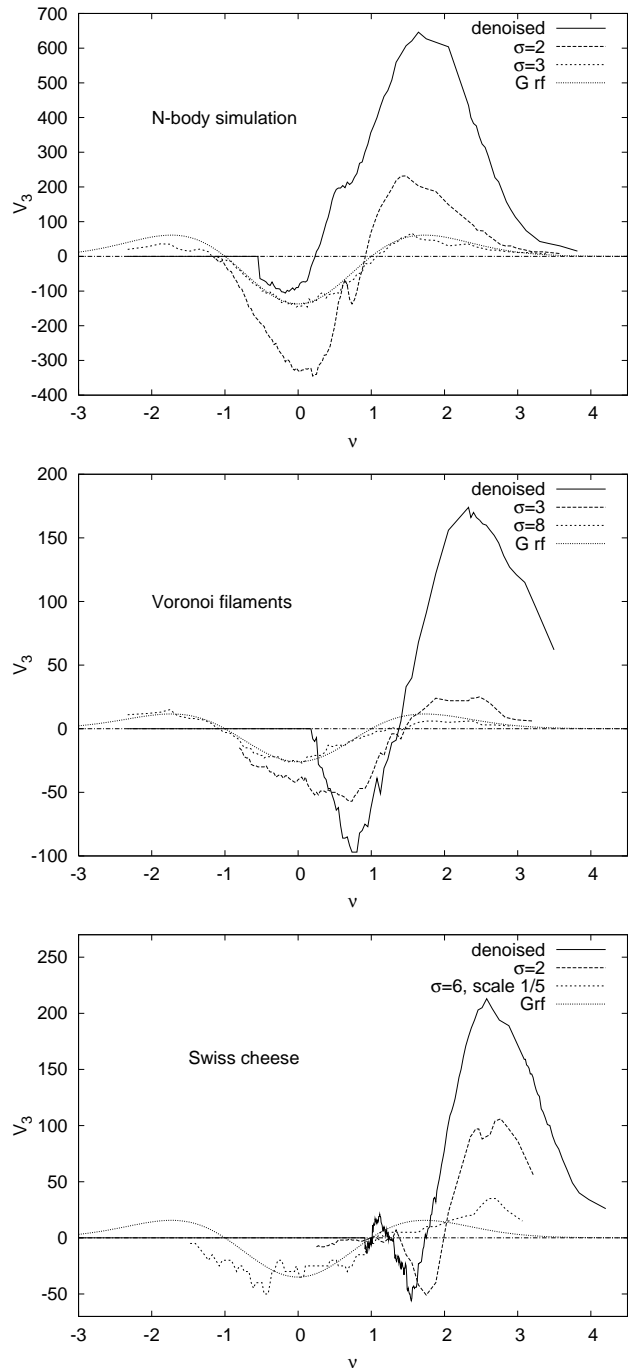


FIG. 5.— The V_3 curves for the three point distributions. We show in each panel the curves obtained by smoothing the data with a Gaussian with two different filter widths (in grid units) and the MF V_3 for the wavelet filtered data set. As previously, the top panel corresponds to the N -Body simulation, the middle panel is for the Voronoi filament model, and the bottom panel corresponds to the nearly-empty Swiss cheese model.

sity of galaxies. Although the catalog does not suffer from luminosity incompleteness, it is slightly spectroscopically incomplete, mainly due to missing galaxies because of fiber collisions. The incompleteness parameter has been determined by every galaxy by the 2dF team; when calculating densities, each galaxy can be weighted by the inverse of this parameter.

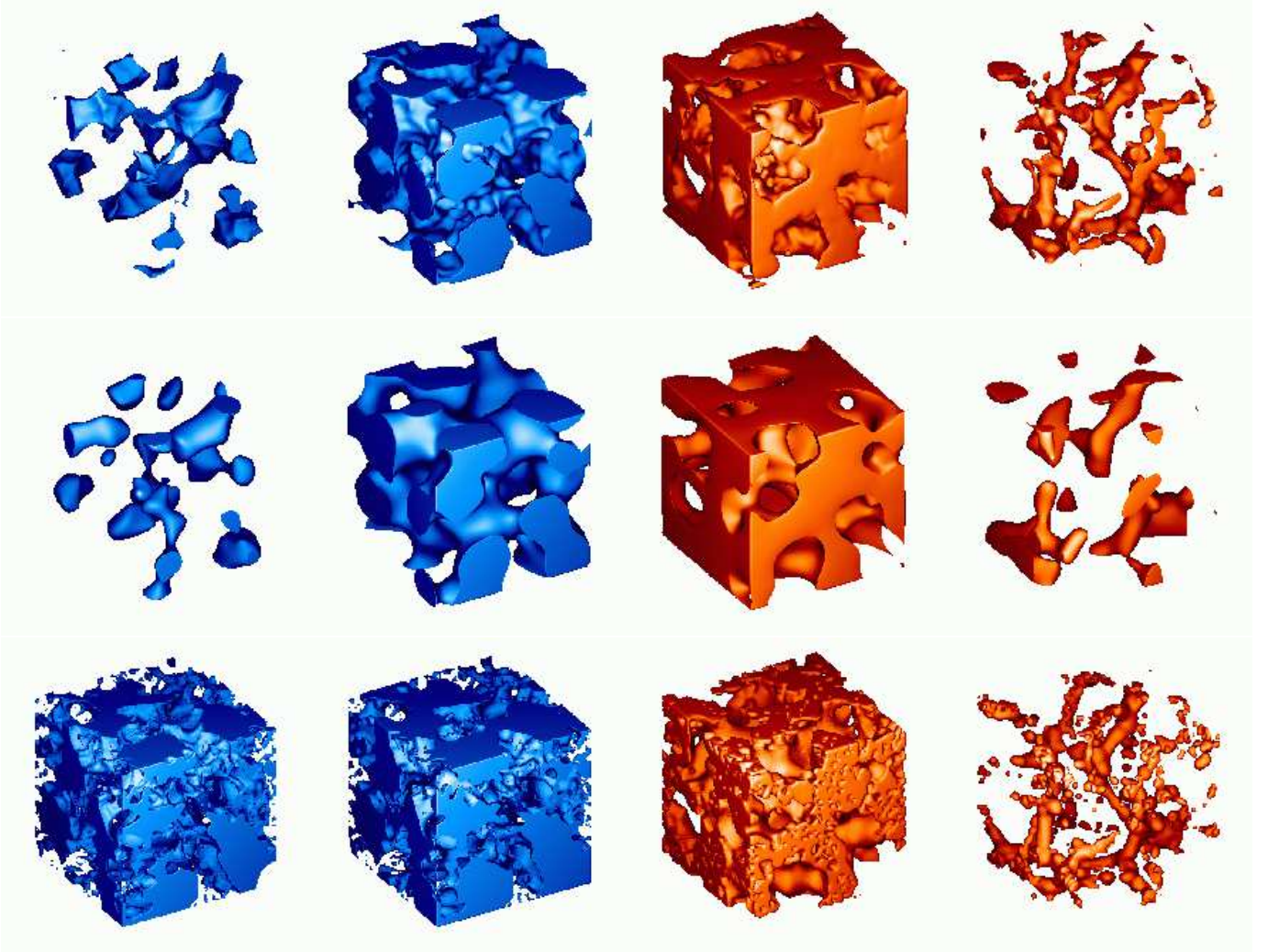


FIG. 6.— The isodensity surfaces corresponding to the Voronoi filament model for the Gaussian-smoothed field with $\sigma = 3$ (upper row), $\sigma = 8$ (middle row, all in grid units) and the wavelet-denoised field (bottom row). The density thresholds delineate, from left to right, 7% low, 50% low, 50% high and 7% high density regions.

We split the volume-limited sample into the Northern and Southern subsamples, and cut off the numerous whiskers in the plane of the sky to obtain compact volumes.

We performed morphological analysis for both the Southern and Northern subsamples. The grid-based scheme we use works well for simple cuboid geometries. The geometry of the Northern sample is similar to a flat slice, while the Southern sample is enclosed between two cones of opening angles of 64.5° and 55.5° . When we tried to cut cuboidal volumes (bricks) from the Southern sample cone, we ended up with small brick volumes. So we carried out the morphological analysis for the full volume of the Southern sample, only to find that the border corrections for the Minkowski functionals are large and uncertain. Thus we report in this paper only the results of the analysis for the Northern sample.

In order to obtain a compact volume, we choose the angular limits for the Northern sample as $-4.5^\circ \leq \delta \leq 2.5^\circ$ and $149.0^\circ \leq \alpha \leq 209.0^\circ$. The slice lies between two cones defined by the δ limits. The right ascension limits cut the cones by planes from both sides, and there

are two additional cuts by two spheres. The radii of the spheres are fixed by the original data, and depend only on the chosen absolute magnitude limits (and on the cosmological model). For our sample they are: $R_1 = 61.1 h^{-1}$ Mpc, $R_2 = 375.6 h^{-1}$ Mpc.

As this sample is pretty flat, we cut from it a maximal volume cuboidal window, a “brick” with dimensions of $254.0 \times 133.1 \times 31.1 h^{-1}$ Mpc, with 8487 galaxies (see Fig. 7). This gives for the per-particle-volume size $d = 5.0 h^{-1}$ Mpc.

5.2. Mock catalogs

In order to estimate sample errors of the Minkowski functionals, we use mock catalogs, provided by the 2dF team. Norberg et al. (2002) created 22 mock catalogs for the 2dFGRS that have been used by the 2dFGRS team to measure the influence of cosmic variance of different statistics, as correlation functions, counts-in-cells, the void probability function, clustering of groups, etc. (Croton et al. 2004a,b; Baugh et al. 2004; Padilla et al. 2004). The mock catalogs were extracted from the Virgo Consortium Λ CDM Hubble volume simulation, and a bi-

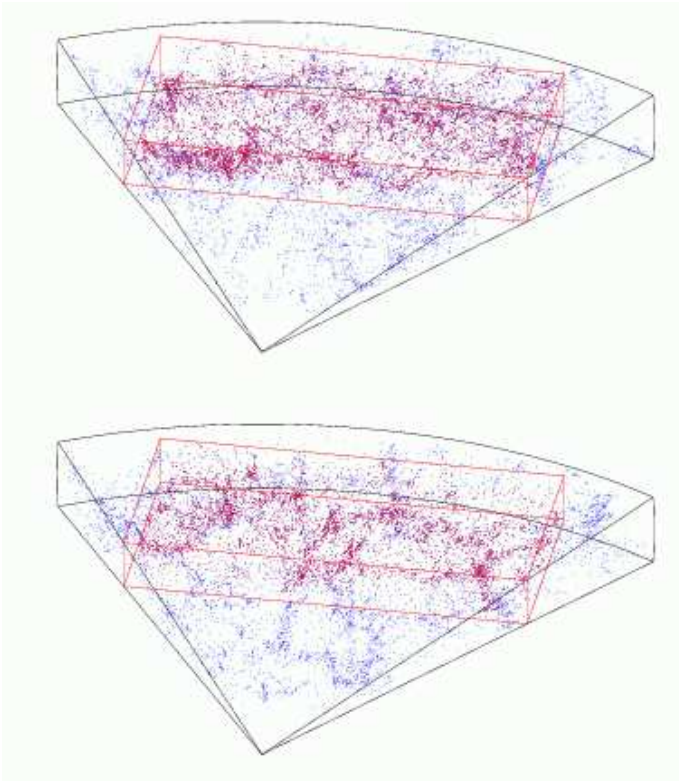


FIG. 7.— The volume-limited cuboidal sample analyzed in this paper drawn from the Northern slice of the 2dFGRS (top) and from a mock realization.

asing scheme described in Cole et al. (1998) was used to populate the dark matter distribution with galaxies. The catalogs were created by placing observers in the Hubble volume, applying the radial and angular selection functions of the 2dFGRS, and translating the positions and velocities of galaxies into redshift space. No luminosity clustering dependence is present in the mock catalogs.

The mock catalogs represent typical volumes of space. The real 2dF catalog, however, includes two superclusters, one in the Northern, another in the Southern subsample (see a thorough discussion in Croton et al. (2004b)). The Northern supercluster is especially prominent in the $M \in [-19, -20]$ survey; all mock samples for this catalog have less galaxies than the 2dF sample. We cut mock bricks from the mock samples, too, as we did for the real 2dF data; the mean number of galaxies in the mock bricks is 1.36 times smaller than in the 2dF brick. The supercluster shows up in the correlation function, too, enhancing correlations at intermediate scales, compared to those of the mocks (Fig. 8). The correlation length for the brick is $r_0 = 6.8 h^{-1}$ Mpc, only slightly larger than the characteristic length $d = 5.0 h^{-1}$ Mpc. We remind the reader that this is the correlation length for redshift space; the 2dF correlation length for real space has been estimated as $R_0 = 5.05 h^{-1}$ Mpc (Hawkins et al. 2003). The mean nearest-neighbor distance is $2.3 h^{-1}$ Mpc, showing that the galaxy distribution is well clustered.

5.3. Minkowski functionals of the 2dFGRS Northern sample

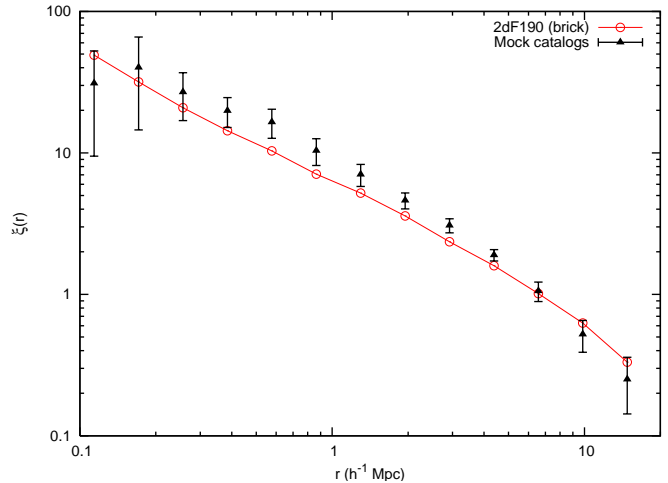


FIG. 8.— The two-point correlation function of the 2dF brick (open circles) together with the average and the total deviation range for the 22 mock catalogs.

As we said, we show the results for only one volume-limited subsample of the 2dFGRS Northern area. Other subsamples have either smaller volumes or smaller galaxy densities.

We do not use the weights to correct for spectroscopic incompleteness for the final results. We have seen that the influence of the weights in the correlation function $\xi(r)$ is negligible. A similar test has been performed by Croton et al. (2004a) using counts-in-cells statistics on mock catalogs, both complete and incomplete, reaching a similar conclusion. We have tested the influence of the incompleteness by calculating density fields for several Gaussian smoothing lengths with and without the weights, and compared the resulting Minkowski functionals. The differences were almost imperceptible, thus we decided for the conceptually simpler procedure.

We calculate the Minkowski functionals by sweeping over the grid (we use a $1 h^{-1}$ Mpc grid step). We start at the nearby border planes, and we account for the edge effects for bricks by not using the grid vertices at the faraway borders. We tested this procedure by using realizations of Gaussian random fields; although the border effects are small, the correction works well. We estimate the significance of the deviations of the MF curves from those for a Gaussian random field, by calculating them for a large number of Gaussian realizations (about 1300). In order to create these realizations, we adopted the analytical approximation for the power spectrum by Klypin & Holtzman (1997), for parameters similar to the concordance model ($\Omega_{\text{matter}} = 0.3, \Omega_{\Lambda} = 0.7, \Omega_{\text{bar}} = 0.026, h = 0.7$).

In order to estimate the cosmic variance, we use the 22 mock bricks described above. As the distribution of MF amplitudes is rather asymmetric, we do not find the variance, but we show the total range of variation of the mock MF curves. As there are 22 mock samples, this range is close to the usual Gaussian “2 sigma” confidence regions. Thus, the confidence regions for Gaussian realizations given in the figures, are also given for the 2σ (95%) level.

We noticed above that the mock catalogs miss the su-

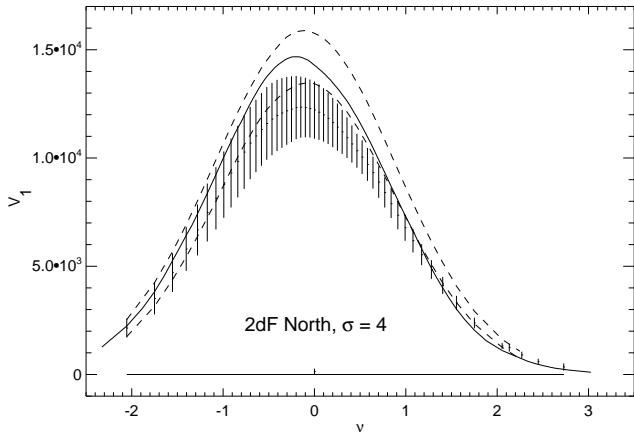


FIG. 9.— The Minkowski functional V_1 for the 2dF GRS Northern brick, for Gaussian smoothing with $\sigma = 4h^{-1}\text{Mpc}$ (solid line). The cosmic error is characterized by the variability of V_1 for 22 mock samples (shown by bars, the same smoothing). The 95% confidence regions for the theoretical prediction, $\sigma = 4h^{-1}\text{Mpc}$ -smoothed realizations of Gaussian random fields with the ‘concordance cosmology’ power spectrum, are shown by dashed lines.

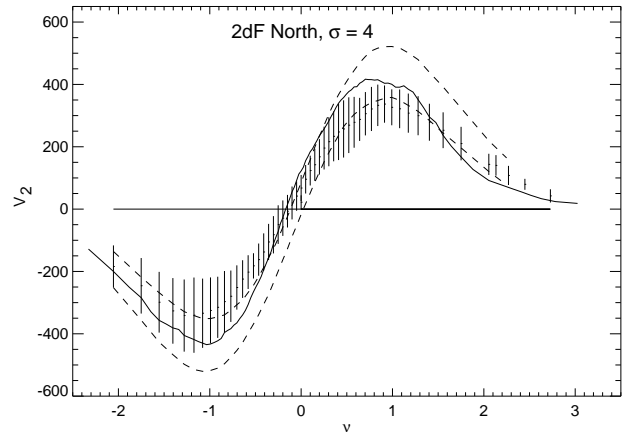


FIG. 10.— The Minkowski functional V_2 for the 2dF GRS Northern brick, for Gaussian smoothing with $\sigma = 4h^{-1}\text{Mpc}$ (solid line). The cosmic error is characterized by the variability of V_2 for 22 mock samples (shown by bars, the same smoothing). The 95% confidence regions for the theoretical prediction, $\sigma = 4h^{-1}\text{Mpc}$ -smoothed realizations of Gaussian random fields with the ‘concordance cosmology’ power spectrum, are shown by dashed lines.

percluster present in the real 2dF sample (look at the front left region of the 2dF brick in the upper panel of Fig. 7), and have systematically lower density than the real 2dF sample. The fix adopted by Croton et al. (2004b) was to cut out the region surrounding the supercluster. We cannot do that, as this would lead to complex boundary corrections. For wavelet cleaning this should not be a problem, the algorithm will automatically follow the density distribution. For Gaussian smoothing, we compensated for the density difference by using 1.11 times wider smoothing lengths for mocks than for the 2dF brick. The smoothing lengths for the Gaussian realization remain unscaled, of course.

We start with the first two nontrivial Minkowski functionals (the first MF, V_0 , is trivially Gaussian due to our choice of the argument ν). The second (Fig. 9) MF (the area of the isodensity surfaces) for the Gaussian smoothing with $\sigma = 4$ (grid units or $h^{-1}\text{Mpc}$) barely fits into the 95% Gaussian confidence interval (it lies completely in the 3σ interval). It is interesting that the values of V_1 for the mocks lie mostly outside of it – the isodensity surfaces are smoother than for the real data (recall the supercluster), and than for the Gaussian random field, too.

The third (Fig. 10) MF (the mean curvature of the isodensity surfaces) for the Gaussian smoothing with the same $\sigma = 4$ as above also lies a bit outside of the 95% Gaussian confidence interval, but fits completely in the 3σ interval, not shown in the figure. Mocks do not lie well within the 95% confident Gaussian band, while the V_2 curve for the 2dF data lies close to the extreme V_2 values of the mock catalogues shown by bars in the diagram. These two figures show that Gaussian smoothing with $\sigma = 4$ (recall that $r_0 = 6.8h^{-1}\text{Mpc}$ for the 2dF brick) has already given a nearly Gaussian morphology to the data.

As usual, the V_3 curves (Fig. 11) show the most details. The upper panel shows that the data smoothed with a Gaussian filter of width $\sigma = 2$, is yet undersmoothed,

but does not differ very much from a Gaussian random field. Discreteness effects are more evident for the mock samples (the peak around $\nu = 0.7$). The middle panel demonstrates again that the density field smoothed with a Gaussian filter of width $\sigma = 4$ can already be considered Gaussian, and the mocks do not differ much from Gaussian realizations either.

These two panels show how the answer to the question of whether the density distribution has intrinsically Gaussian morphology, depends on the adopted smoothing widths. The bottom panel shows the result for wavelet filtering of the point distribution. This curve is clearly non-Gaussian, showing the presence of compact clusters for high-density isosurfaces, and a sponge-like morphology near $\nu = 0$. However, in contrast to the Gaussian case, the curve returns to 0 for smaller values of ν – about half of the sample space remains empty after wavelet denoising. Gaussian smoothing, on the contrary, tends to fill up the space. The wavelet-filtered mocks show, in principle, similar behavior to the data. They are only smoother, as seen from the differences around $\nu = 2$. It is interesting that the wavelet-filtered V_3 curve is similar to those for the Voronoi filament sample – both samples are filamentary at larger scales. Wavelet morphology returns a clear picture of the density field, again, in contrast to the Gaussian-smoothed V_3 for the 2dF data, where filamentarity is difficult to see.

6. CONCLUSIONS

We have presented a new wavelet-based method to study the morphology of the galaxy distribution – wavelet morphology. As we have shown, it gives a unique morphological description, and is more accurate, capturing the details of the distribution that are destroyed by usual Gaussian smoothing. The code for the analysis of wavelet morphology will be made available at <http://jstarck.free.fr>.

Using special highly non-Gaussian realizations of point processes, we have demonstrated that Gaussian smooth-

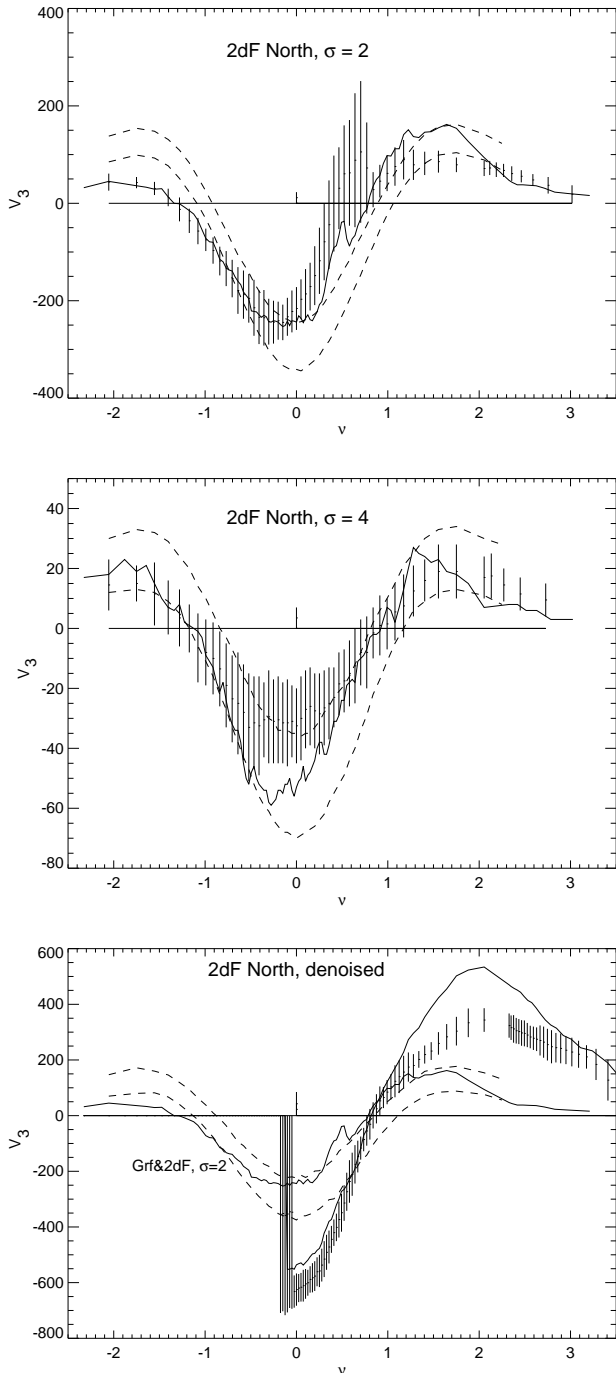


FIG. 11.— The Minkowski functional V_3 for the 2dF brick. The upper panels show the results for Gaussian smoothing with $\sigma = 2h^{-1}\text{Mpc}$ and $\sigma = 4h^{-1}\text{Mpc}$, respectively (the designations are the same as in the previous two figures). The bottom panel describes wavelet morphology of the 2dF GRS, showing the V_3 curve for the wavelet denoised data set (thick solid line), and comparing it with the variability range of the wavelet denoised mocks (bars). We show also the 95% confidence limits for 1300 realizations of theoretical Gaussian density fields (dashed lines), and the V_3 data curve (thin solid line), all obtained for the Gaussian $\sigma = 2h^{-1}\text{Mpc}$ smoothing.

ing introduces Gaussian features in the morphology, and is thus not the best tool to search for departures from Gaussianity.

We performed wavelet-morphological analysis of the most detailed 2dF GRS volume-limited sample and found that it is clearly non-Gaussian. The wavelet Minkowski functional V_3 finds high-density clusters, large-scale filamentarity, and huge empty voids. A similar morphological analysis, based on Gaussian smoothing, leads to the conclusion that the morphology of the sample is close to Gaussian, already for comparatively small smoothing lengths ($\sigma \geq 4h^{-1}\text{Mpc}$). This is a clear example of Gaussian contamination.

The isotropic wavelet transform is optimal only for the detection of isotropic features, but not for the detection of filaments or walls. A clear improvement could be made by using simultaneously several other multiscale transforms such the ridgelet transform and the beamlet transform which are respectively well suited for walls and filaments (Starck et al. 2005). This will be done in the future.

Wavelet morphology detects also the large supercluster in the 2dFGRS Northern sample, that has not been modeled by N -body mock catalogs. A signature of the presence of this supercluster could be deduced from the correlation function. Gaussian morphology does not detect this feature.

We thank Rien van de Weigaert for his Voronoi program, Darren Croton for providing us with the 2dF volume-limited data and explanations and suggestions on the manuscript, and Peter Coles for discussions. This work has been supported by the University of Valencia through a visiting professorship for Enn Saar, by the Spanish MCyT project AYA2003-08739-C02-01 (including FEDER), by the Generalitat Valenciana project GRUPOS03/170, by the National Science Foundation grant DMS-01-40587 (FRG), and by the Estonian Science Foundation grant 6104.

REFERENCES

- Adler, R. J. 1981, *The Geometry of Random Fields*, (New York: John Wiley & Sons)
- Antoniadis A., & Sapatinas, T. 2001, *Biometrika*, 88, 805
- Baugh, C. M., et al. 2004, *MNRAS*, 351, L44
- Cole, S., Hattton, S., Weinberg, D. H., & Frenk, C. S., 1998, *MNRAS*, 300, 945

- Coles, P., Davies, A. G., & Pearson, R. C. 1996, MNRAS, 281, 1375
- Coles, P. & Lucchin, F., 1995, *Cosmology: The Formation and Evolution of Cosmic Structure* (New York: John Wiley & Sons)
- Colless, M., et al. 2003, astro-ph/0306581
- Croton, D. J., et al. 2004, MNRAS, 352, 828
- Croton, D. J., et al. 2004, MNRAS, 352, 1232
- Donoho, D. L., 1988, *Ann. Statist.*, 16, 1390
- Fryźlewicz, P. & Nason, G. P. 2004, *J. Comp. Graph. Stat.*, 13, 621
- Gott, J. R., Dickinson, M., & Melott, A. L. 1996, *ApJ*, 306, 341
- Hamilton, A. J. S., Gott, J. R. I., Weinberg, D. 1996, *ApJ*, 309, 1
- Hawkins, E. et al. (the 2dFGRS Team), 2003, MNRAS, 346, 78
- Hoyle, F., et al., 2002, *ApJ*, 580, 663
- Jammal, G., & Bijaoui, A., 2004, *Signal Process.*, 84(7), 1049
- Kerscher, M., et al. 1997, MNRAS, 284, 73
- Klypin, A., & Holtzman J. 1997, astro-ph/9712217
- Kolaczyk, E. D. 1999, *Statist. Sinica*, 9, 119
- Kolaczyk, E. D. 2000, *ApJ*, 534, 490
- Martínez, V. J., Paredes, S., & Saar, E. 1993, MNRAS, 260, 365
- Martínez, V. J., & Saar, E. 2002, *Statistics of the Galaxy Distribution*, (Boca-Raton: Chapman & Hall/CRC press)
- Mecke K. R., Buchert, T., & Wagner, H. 1994, *A&A*, 288, 697
- Minkowski, H., 1903, *Mathematische Annalen* 57, 447
- Norberg, P., et al. 2002, MNRAS, 336, 907
- Nowak, R. D., & Baranuik, R. G. 1999, *IEEE Transactions on Image Processing*, 8(5), 666
- Padilla, N. D., et al. 2004, MNRAS, 352, 211
- Pierre, M., et al. 2004, *Journal of Cosmology and Astro-Particle Physics*, 9, 11
- Schmalzing J., & Buchert, T. 1997, *ApJ*, 482, L1
- Schmalzing J., Kerscher M. and Buchert T. (1996), in *Dark Matter in the Universe*, eds. S. Bonometto, J.R. Primack & A. Provenzale, (Amsterdam: IOS Press), 281
- Sheth, J. V., & Sahni, V. 2005, astro-ph/0502105
- Sheth, J. V., Sahni, V., Shandarin, S. F., & Sathyaprakash, B. S., 2003, MNRAS, 343, 22
- Silverman B. W. 1981, *J. R. Statist. Soc. B*, 43, 97
- Silverman B. W. 1986, *Density Estimation for Statistics and Data Analysis*, (London: Chapman & Hall)
- Slezak, E., de Lapparent, V., & Bijaoui, A. 1993, *ApJ*, 409, 517
- Starck, J.-L., & Murtagh, F. 2002, *Astronomical Image and Data Analysis*, (Berlin: Springer-Verlag)
- Starck, J.-L., Murtagh, F. & Bijaoui, A. 1998, *Image Processing and Data Analysis: The Multiscale Approach*, (Cambridge: Cambridge University Press)
- Starck, J.-L., Pierre, M. 1998, *A&AS*, 128, 397
- Starck J.-L., Bijaoui, A., Murtagh, F., 1995, *CVGIP: Graphical Models and Image Processing*, 57, 420.
- Starck, J.-L., Martínez, V. J., Donoho, D. L., Levi, O., Querre, P. & Saar, E. 2005, *Eurasip Journal of Signal Processing* (in press)
- Timmermann, K. E., & Nowak, R. D. 1999, *IEEE Transactions on Information Theory*, 45(3), 846
- Tomita, H., 1990, in *Formation, Dynamics and Statistics of Patterns* eds. K. Kawasaki, et al., Vol. 1, (World Scientific), 113
- Valtchanov, I., Pierre, M., & Gastaud, R. 2001, *A&A*, 370, 689
- Valtchanov, I., et al. 2004, *A&A*, 423, 75